TEMPERATURE STRUCTURE AND METALLICITY IN H II REGIONS

Mónica Rodríguez[1] and Jorge García-Rojas[2,3,4]

[1] Instituto Nacional de Astrofísica, Óptica y Electrónica, Apdo Postal 51 y 216, 72000 Puebla, Mexico; mrodri@inaoep.mx
[2] Instituto de Astronomía, Universidad Nacional Autónoma de México, Apdo Postal 70-264, 04510 México DF, Mexico; jogarcia@iac.es

ABSTRACT

The metallicities implied by collisionally excited lines (CELs) of heavy elements in H II regions are systematically lower than those implied by recombination lines (RLs) by factors of ~ 2, introducing uncertainties of the same order in the metallicities inferred for the interstellar medium of any star-forming galaxy. Most explanations of this discrepancy are based on the different sensitivities of CELs and RLs to electron temperature, and invoke either some extra heating mechanism producing temperature fluctuations in the ionized region or the addition of cold gas in metal-rich inclusions or ionized by cosmic rays or X-rays. These explanations will change the temperature structure of the ionized gas from the one predicted by simple photoionization models, and depending on which one is correct, will imply different metallicities for the emitting gas. We select nine H II regions with observed spectra of high quality and show that simple models with metallicities close to the ones implied by oxygen CELs reproduce easily their temperature structure, measured with $T_e([N\,II])/T_e([O\,III])$, and their oxygen CELs emission. We discuss the strong constraints that this agreement places on the possible explanations of the discrepancy and suggest that the simplest explanation, namely errors in the line recombination coefficients by factors ~ 2, might be the correct one. In such case, CELs will provide the best estimates of metallicity.

Key words: H II regions – ISM: abundances

Online-only material: color figures

1. INTRODUCTION

In an H II region, the temperature of a volume of gas in thermal equilibrium is determined by the balance between heating, mainly through photoionization, and cooling, mainly through recombination and radiation of collisionally excited lines (CELs). The most important coolants are CELs arising from low-energy levels of ions of abundant metals, like O^+, O^{++}, N^+, S^+, and S^{++}, and the gas metallicity is the single most important parameter in the determination of the final temperature of the gas (Osterbrock & Ferland 2006).

Temperatures can be measured using the relative intensities of CELs emitted by ions like O^{++} and N^+, and their associated temperatures, $T_e([O\,III])$ and $T_e([N\,II])$, can be used to characterize the zones of high and low degree of ionization within a nebula. These temperatures can be used to calculate line emissivities and hence the abundances of different elements. The oxygen abundance is probably the most reliable one that can be derived in H II regions; and it is generally used as a proxy for the metallicity of the gas. When optical spectra of high quality are available, the oxygen abundance is derived by adding the O^+/H^+ and O^{++}/H^+ abundance ratios implied by the intensities of optical [O II] and [O III] lines (relative to hydrogen recombination lines) and the corresponding emissivities calculated for $T_e([N\,II])$ and $T_e([O\,III])$, respectively. However, the O^{++} abundance can also be determined using several weak optical O II recombination lines (RLs) and these lead to abundances that are consistently higher than the ones derived from CELs. A similar result has been found with CELs and RLs of other ions, both in H II regions and in planetary nebulae (see, e.g.,

Esteban et al. 2004; Liu et al. 2004), but with higher uncertainties. The abundance discrepancy factors (ADFs) for O^{++}, $\text{ADF}(O^{++}) = (O^{++}/H^+)_{RL}/(O^{++}/H^+)_{CEL}$, are of the order of 2 for H II regions and many planetary nebulae, but can reach much higher values, up to 70, in the latter objects (Liu 2006 and references therein).

Most of the proposed explanations of the ADF are based on the different dependence with temperature of the emissivities of CELs (strongly increasing with T_e) and RLs ($\propto T_e^{-m}$ with $m \simeq 1$). If there are large temperature fluctuations in the gas, the emission of CELs will be heavily weighted toward the hotter regions, and the emission of RLs toward the colder ones. Depending on the mechanism responsible for the fluctuations, either CELs or RLs will provide the better estimate of the gas metallicity. The fluctuations could be due to hot gas heated by shocks, stellar winds, small dust grains, magnetic reconnection (see Torres-Peimbert & Peimbert 2003 and references therein), or can be due to cold gas in metal-rich inclusions (Liu et al. 2000; Tsamis & Péquignot 2005; Stasińska et al. 2007) or cold gas ionized by cosmic rays (Giammanco & Beckman 2005) or X-rays (Ercolano 2009). Some or all of these effects are likely to be present in real objects, but it is not clear yet whether they can explain the derived ADFs or how much they contribute to the observed emission. This introduces an uncertainty in the absolute values of the metallicities in the interstellar medium (ISM).

One way to approach this issue, the one we will follow here, is to build a series of simple photoionization models with input parameters that can be considered representative of some observed objects and to see whether the models reproduce the observed spectra. We center on nine H II regions with available spectra of high quality and use Cloudy (Ferland et al. 1998) to calculate grids of photoionization models that depend only on a few free parameters. The observed and predicted spectra are analyzed in a similar way to determine electron densities,

---

[3] Visiting Astronomer, Instituto Nacional de Astrofísica, Óptica y Electrónica, Apdo Postal 51 y 216, 72000 Puebla, Mexico.
[4] Current address: Instituto de Astrofísica de Canarias, E-38200 La Laguna, Tenerife, Spain.

Table 1
Physical Conditions and Oxygen Abundances for the Sample Objects

Object	n_e (cm^{-3})	T_e ([N II]) (K)	T_e ([O III]) (K)	$12 + \log$ (O/H)	$\log$ (O$^+$/O^{++})	ADF (O^{++})
M8	1550 ± 150	8500 ± 120	8020 ± 100	8.44 ± 0.03	$+0.40 \pm 0.05$	2.2 ± 0.2
M16	980 ± 120	8500 ± 150	7580 ± 150	8.52 ± 0.03	$+0.45 \pm 0.06$	2.4 ± 0.6
M17	420 ± 80	9150 ± 250	7950 ± 100	8.53 ± 0.02	-0.76 ± 0.06	1.8 ± 0.2
M20	220 ± 40	8500 ± 150	7750 ± 250	8.48 ± 0.03	$+0.64 \pm 0.07$	1.9 ± 1.2
M42	6800 ± 600	10100 ± 250	8250 ± 60	8.53 ± 0.02	-0.68 ± 0.05	1.50 ± 0.05
NGC 2467	260 ± 50	9600 ± 200	8900 ± 100	8.35 ± 0.03	$+0.35 \pm 0.05$	1.8 ± 0.2
NGC 3576	1400 ± 200	8950 ± 200	8400 ± 80	8.53 ± 0.02	-0.40 ± 0.06	2.0 ± 0.3
NGC 3603	2350 ± 400	11650 ± 570	9000 ± 150	8.47 ± 0.03	-1.21 ± 0.09	1.9 ± 0.3
30 Doradus	380 ± 50	10800 ± 300	9850 ± 100	8.36 ± 0.02	-0.77 ± 0.06	1.5 ± 0.1

temperatures, and the ionic and total abundances of oxygen using the intensities of CELs relative to hydrogen lines. We show that the models reproduce easily the general trends defined by the observations. We argue that they are representative of the observed objects and discuss how far they can be modified by adding some extra ingredient that could also explain the intensities of O II RLs without destroying the agreement.

2. THE OBSERVATIONAL SAMPLE

We consider nine H II regions with published spectra of the best quality: the Galactic H II regions M42 (Esteban et al. 2004), NGC 3576 (García-Rojas et al. 2004), NGC 2467 (García-Rojas et al. 2005), M16, M20, NGC 3603 (García-Rojas et al. 2006), M8, M17 (García-Rojas et al. 2007), and 30 Doradus (Peimbert 2003) in the Large Magellanic Cloud (LMC). Deep spectra of these nebulae were obtained with the Very Large Telescope (VLT) UVES echelle spectrograph covering the range 3100–10400 Å with spectral resolution of $\Delta\lambda \simeq 8800/\lambda$. The spectra, which were extracted over small fractional areas, $3'' \times 8''.5$ or $3'' \times 10''$, allowed the measurement of 235–555 emission lines in each nebula, including several weak O II ORLs that were detected with good signal-to-noise ratios. Physical conditions could be derived from several diagnostics that led to broadly consistent values.

Since we will be comparing the values of the temperatures and abundances derived from the observed spectra with those derived from the line intensities predicted by the photoionization models, we decided to use the same atomic data for all calculations. Hence, we recomputed the parameters of interest with the *nebular* package in IRAF[5] but using the same atomic data as Cloudy. This implied changing the tables of transition probabilities and collision strengths used in IRAF for the elements of interest (references for the values we used for these atomic data can be found in García-Rojas et al. 2009). We neither changed the number of levels used in the calculations nor the procedure used by IRAF to get the emissivities of the hydrogen lines, but the effects of these differences are small.

The recomputed electron densities, n_e, are a weighted mean of the values implied by the diagnostics [S II] $\lambda6716/\lambda6731$, [O II] $\lambda3726/\lambda3729$, and [Cl III] $\lambda5517/\lambda5537$. The values of T_e([O III]) are based on the ratio of line intensities ($\lambda4959 + \lambda5007$)/$\lambda4363$; those of T_e([N II]) on ($\lambda6548 + \lambda6583$)/$\lambda5755$. In some of the previous studies, the values of T_e([N II]) were corrected for the contribution of recombination to the intensity of [N II] $\lambda5755$ (Rubin 1986), but since the corrections are based

on uncertain estimates of the abundance of N^{++}, we prefer to apply that correction to the models (see Section 3). The values of I([O II] $\lambda3726+29$)/I(Hβ), n_e, and T_e([N II]) are used to derive the O$^+$/H$^+$ abundance ratio; I([O III] $\lambda4959 + \lambda5007$)/$I$(H$\beta$), n_e, and T_e([O III]) are used for O^{++}/H$^+$. The total abundance of oxygen is then obtained from the sum of the O$^+$ and O^{++} ionic abundances. We also recomputed the O^{++} abundances implied by RLs using the O II multiplet 1 and the recombination coefficients of Péquignot et al. (1991), which are those implemented in Cloudy. In Table 1, we show the physical conditions, T_e, n_e, and the degree of ionization, the O/H abundances derived from CELs and the ADFs for all the sample objects. Despite the slight changes in the procedure and in the atomic data used, the final values of the oxygen abundance and of the ADF are consistent within the errors with the values derived in the previous analyses.

3. THE PHOTOIONIZATION MODELS

Calculations were performed with version 08.00 of Cloudy, last described by Ferland et al. (1998). Taking into account that the observations covered small fractional areas of the objects, that different ions lead to similar densities, and that the line emissivities are roughly proportional to the square of the density, one-dimensional plane-parallel models with constant density should be a good approximation.

We use models with total hydrogen densities close to the electron densities derived for the observed objects: $n_H = 300$ cm^{-3} for M17, M20, 30 Doradus, and NGC 2467; $n_H = 1000$ cm^{-3} for NGC 3576, M8, and M16; and $n_H = 5000$ cm^{-3} for NGC 3603 and M42.

We define the ionizing radiation field through two parameters: the effective temperature of the ionizing star, $T_{\rm eff}$, and the ionization parameter $u = \phi_H/n_H c$, with ϕ_H as the number of hydrogen ionizing photons arriving at the inner face of the cloud per unit area and unit time, and c as the speed of light.

We consider the two sets of state-of-the-art model atmospheres for O-type stars included in Cloudy: WM-BASIC (Pauldrach et al. 2001) and TLUSTY (Lanz & Hubeny 2003). Comparisons between the ionizing fluxes predicted by different stellar models and discussions on the effects on the resulting photoionization models can be found in Martins et al. (2005), Simón-Díaz & Stasińska (2008), or in the references therein. Here, we present the results obtained with WM-BASIC and use the results obtained with TLUSTY as a check for robustness. We use stellar models with surface gravity log $g = 4.0$, solar metallicity, and effective temperatures $T_{\rm eff} = 35,000, 37,000, 39,000, 41,000, 43,000, 45,000,$ and 50,000 K. The stellar models with $T_{\rm eff} = 35,000$ K–45,000 K represent roughly the spectral types

---

[5] IRAF is distributed by NOAO, which is operated by AURA, Inc., under cooperative agreement with NSF.

from O3 to O8 (Martins et al. 2005); the models with $T_{eff} =$ 50,000 K probe the effects of more massive stars. The values of u are chosen for each value of T_{eff} so that the set of models cover the range of degrees of ionization found for the observed objects. For the models with $n_H = 300$ and 1000 cm^{-3}, we use log $u = -1.5, -1.0, -0.5,$ and 0.0 for $T_{eff} = 35,000$ K; log $u = -2.5, -2.0, -1.5,$ and -1.0 for $T_{eff} = 37,000$ K; log $u = -3.0, -2.5, -2.0,$ and -1.5 for $T_{eff} = 39,000$ K; and log $u = -3.5, -3.0, -2.5,$ and -2.0 for $T_{eff} = 41,000,$ 43,000, 45,000, and 50,000 K. For the models with $n_H = 5000$ cm^{-3}, we increased the values of log u by 0.5 dex.

We also computed models ionized by two stars with $T_{eff} = 35,000$ and 45,000 K that provide equal amounts of hydrogen ionizing photons (log $u = -3.3, -2.8, -2.3,$ or -1.8 for each star). These models illustrate the effect of a composite stellar radiation field.

We use the set of abundances labeled as "H II region" (or "Orion") in Cloudy and the associated "H II region" dust grains. We scaled both metals and grains in the "H II region" set by the same factor in order to explore different metallicities. We changed the metallicity using steps of 0.1 dex and explored the range $12 + \log(O/H) = 8.3–9.1$.

By default, Cloudy stops when the model reaches an electron temperature of 4000 K. However, since some of the models with high metallicity reach this temperature in the fully ionized zone, we switched off this criterion and used instead the condition $\log(n_e/n_H) \leqslant -0.5$.

For each model, we get a list with the intensities relative to Hβ of the lines of interest. We introduce this list in IRAF and use it to calculate physical conditions and ionic abundances following the same procedure we used in the analysis of the observed objects (see Section 2).

As mentioned in Section 2, the upper level of the [N II] $\lambda 5755$ line used to derive T_e([N II]) can be populated by recombination processes (Rubin 1986). If this effect is not taken into account, the values of T_e([N II]) derived for the models will be lower than those derived for the observed objects, especially for the cases where the degree of ionization is high. Liu et al. (2000) estimated the contribution to the intensity of this line in terms of the N^{++} abundance. We used their correction to add this contribution to the intensity of the [N II] in each model using the N^{++} and H$^+$ column densities and $T_e = 10,000$ K (the dependence on T_e is very weak). Then, we calculated a second set of physical conditions and abundances for all the models. Since the correction is just an estimate, both the corrected and uncorrected results are shown below.

4. RESULTS

We compared the physical conditions and abundances derived for the models with those derived for the observed objects. Most of the models lead to derived abundances, (O/H)$_{out}$, that are lower than the input ones. This is a well-known effect (Stasińska 2005 and references therein), due to the exponential dependence with temperature of the CELs used to derive T_e and the O$^+$ and O^{++} abundances. In the presence of a temperature gradient, this dependence leads to an overestimation of T_e and hence of the emissivity of the CELs. This translates into an underestimation of the derived abundances relative to hydrogen. As discussed by Stasińska (2005), under some circumstances, models with high metallicity and low density develop a gradient so steep that the difference between the input (O/H) and (O/H)$_{out}$ becomes substantial. One extreme case is our model with $n_H = 300$ cm^{-3}, $T_{eff} = 41,000$ K, log $u = -2.0$, and $12 + \log(O/H) = 9.1$. The

abundance derived from the analysis of the spectrum predicted for this model is $12 + \log(O/H)_{out} = 8.55$, and ADF(O^{++}) $\simeq 4$. Other high-metallicity models have ADFs close to the ones derived for the observed objects, but also T_e([O III]) $\lesssim 6000$ K, much lower than the observed values. All the models that consistently give values of (O/H)$_{out}$, T_e([N II]), and T_e([O III]) close to the observed ones, have input metallicities 0–0.06 dex higher than the derived ones and ADF(O^{++}) $\simeq 1.1$.

Figures 1 and 2 show a comparison of T_e([O III]) and T_e([N II])/T_e([O III]) as a function of the derived values for the degree of ionization, $\log(O^+/O^{++})$, for models and observations. The results implied by models with two input metallicities are shown for each object: $12 + \log(O/H) = 8.5$ and 8.6 for M8, M16, M17, M20, NGC 3576, M42, and NGC 3603; $12 + \log(O/H) = 8.3$ and 8.4 for NGC 2467 and 30 Doradus. The output metallicities of these models, (O/H)$_{out}$, bracket the observed values listed in Table 1. The observed objects are compared with those models that have similar values of n_e. It can be seen that these models also reproduce easily the temperatures derived for the observed nebulae. An exception is the value of T_e([N II])/T_e([O III]) for NGC 3576. This could be just a statistical fluctuation, with one in nine measurements deviating with a 2σ error bar from the expected result, or could indicate that something is different in the environment of this object.

Note that the models ionized by two stars with $T_{eff} = 35,000$ K and 45,000 K (the pentagons in Figures 1 and 2) give results that are intermediate between those shown by the models ionized by one star with either $T_{eff} = 35,000$ K or 45,000 K (the asterisks and the circles, respectively). Hence, models ionized by composite spectra, with several values of T_{eff}, will also appear in the regions sampled by the single T_{eff} models in Figures 1 and 2.

Very similar results to the ones found with WM-BASIC were obtained using the TLUSTY model atmospheres. Although individual models would appear in somewhat different positions if plotted in Figures 1 and 2, the areas covered by both kinds of models are roughly similar.

Many simplifying assumptions were made constructing these models. The agreement with the observations suggests that despite the simplifications and uncertainties, the models have captured some basic characteristics of the observed objects. We have already addressed the effects of having a composite ionizing spectra and of using different model atmospheres. We now address other uncertainties and simplifications of the models to further explore how general are the results.

4.1. Effect of Intervening Material

Our models assume that there is no intervening material between the ionizing stars and the observed area. However, this material, if present, will change the shape (and luminosity) of the ionizing radiation field reaching the observed region and, in principle, this could lead to departures from the behavior of the models in Figures 1 and 2. To check for this effect, we calculated several models where the stellar radiation field was first passed through a slab of material of fixed depth and the transmitted radiation was then used to ionize the slab of interest.

We start considering intervening material with $n_H = 300$ cm^{-3}, $12 + \log(O/H) = 8.6$, and a radiation field with $T_{eff} = 39,000$ K and log $u = -1.0$. If enough material is present, these conditions will produce a depth of ionized material of about 4 pc. We consider slabs with thicknesses of 1, 2, and 3 pc and use the radiation transmitted through them to ionize material with the same n_H and metallicity. These models have values of
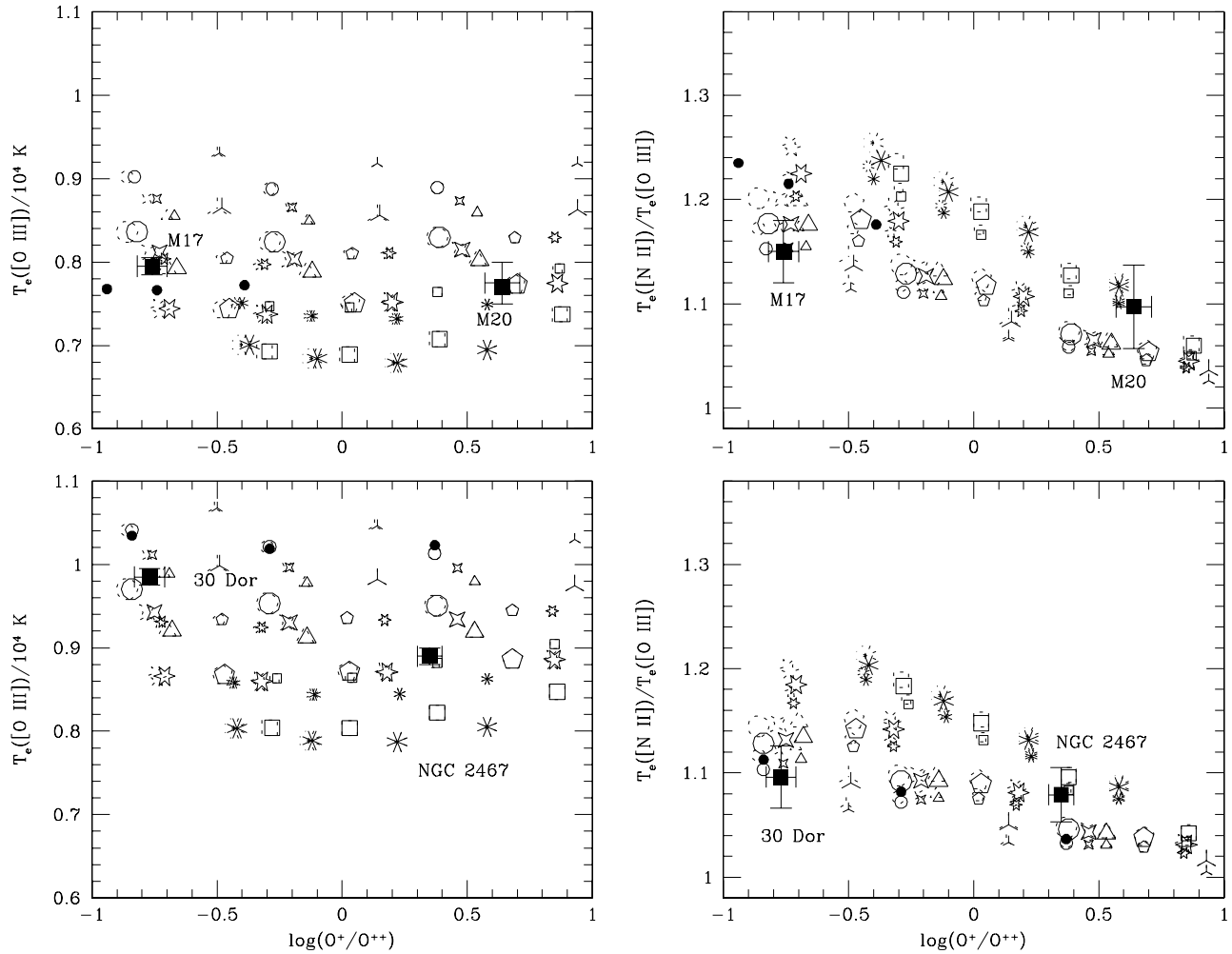
Figure 1. Values of $T_e([O\ III])$ and $T_e([N\ II])/T_e([O\ III])$ for observed objects (filled black squares) and photoionization models (other symbols). The models have $n_H = 300$ cm^{-3} and $T_{eff} = 35{,}000$ K (red asterisks), 37,000 K (orange open squares), 39,000 K (green six-pointed stars), 41,000 K (cyan triangles), 43,000 K (blue four-pointed stars), 45,000 K (violet circles), 50,000 K (black inverted Ys), or both $T_{eff} = 35{,}000$ K and 45,000 K (magenta pentagons). Big symbols correspond to models with $12 + \log(O/H) = 8.6$ (top panels) and 8.4 (bottom panels). Small symbols have $12 + \log(O/H) = 8.5$ (top panels) and 8.3 (bottom panels). Dotted symbols show values derived considering the contribution of recombination to the intensity of [N II] $\lambda 5755$. The small filled circles show the effects of intervening material changing the shape of the ionizing radiation field (top panels, for models with $T_{eff} = 39{,}000$ K and $12 + \log(O/H) = 8.6$) and of decreasing the abundances of C, N, S, and Ne relative to O (bottom panels, for models with $T_{eff} = 45{,}000$ K and $12 + \log(O/H) = 8.4$). See the text for more explanations.

(A color version of this figure is available in the online journal.)

the ionization parameter of $\log u = -1.23$, -1.5, and -1.93, respectively. The spectra produced by the latter slabs were analyzed in the same manner as the original models and the results are plotted as small filled circles in the top panels of Figure 1. It can be seen that they give results similar to the original grid of models.

We calculated similar models (with $12 + \log(O/H) = 8.6$, $T_{eff} = 39{,}000$ K, and initial $\log u = -1.0$) for material with $n_H = 1000$ cm^{-3}. The incident radiation field was first passed through slabs with the same density and depths of 0.3, 0.6, and 0.9 pc (so that for the final models $\log u = -1.23$, -1.5, and -1.9). We did other tests with intervening material of lower density, $n_H = 100$ cm^{-3}, and depths of 1, 2, and 3 pc (leading to $\log u = -1.06$, -1.11, and -1.17 for the final models with $n_H = 1000$ cm^{-3}). All these models also gave similar results to those produced by the original grid of models.

4.2. Changing the Relative Abundances of Some Elements

We are using the set of "H II region" chemical abundances in Cloudy (based on the abundances derived for M42 by Baldwin

et al. 1991; Rubin et al. 1991; Osterbrock et al. 1992) and scaling all of them by the same amount to change the overall metallicity of the gas, which we measure through O/H. For the other elements, not all ionization states show lines in the optical and their total abundances are derived using ionization correction factors that make them less reliable. Changing the abundances relative to oxygen of those elements that contribute significantly to the cooling might change our results. We compared the values of the C/O, N/O, S/O, and Ne/O abundance ratios in Cloudy with the values derived for these ratios in the original papers where the analysis of the observed objects was first presented. The most discrepant results are found for 30 Doradus, with C/O, N/O, S/O, and Ne/O lower than the Cloudy values by 0.4, 0.5, 0.1, and 0.14 dex, respectively. Hence, we ran three new models with $n_H = 300$ cm^{-3}, $12 + \log(O/H) = 8.4$, $T_{eff} = 45{,}000$ K, $\log u = -3.0$, -2.5, and -2.0, and with the abundances of C, N, S, and Ne scaled down by the amounts listed above. The results are shown as small filled circles in the bottom panels of Figure 1. As expected, they show somewhat higher values of T_e, but the values of $T_e([N\ II])/T_e([O\ III])$ do not change significantly.
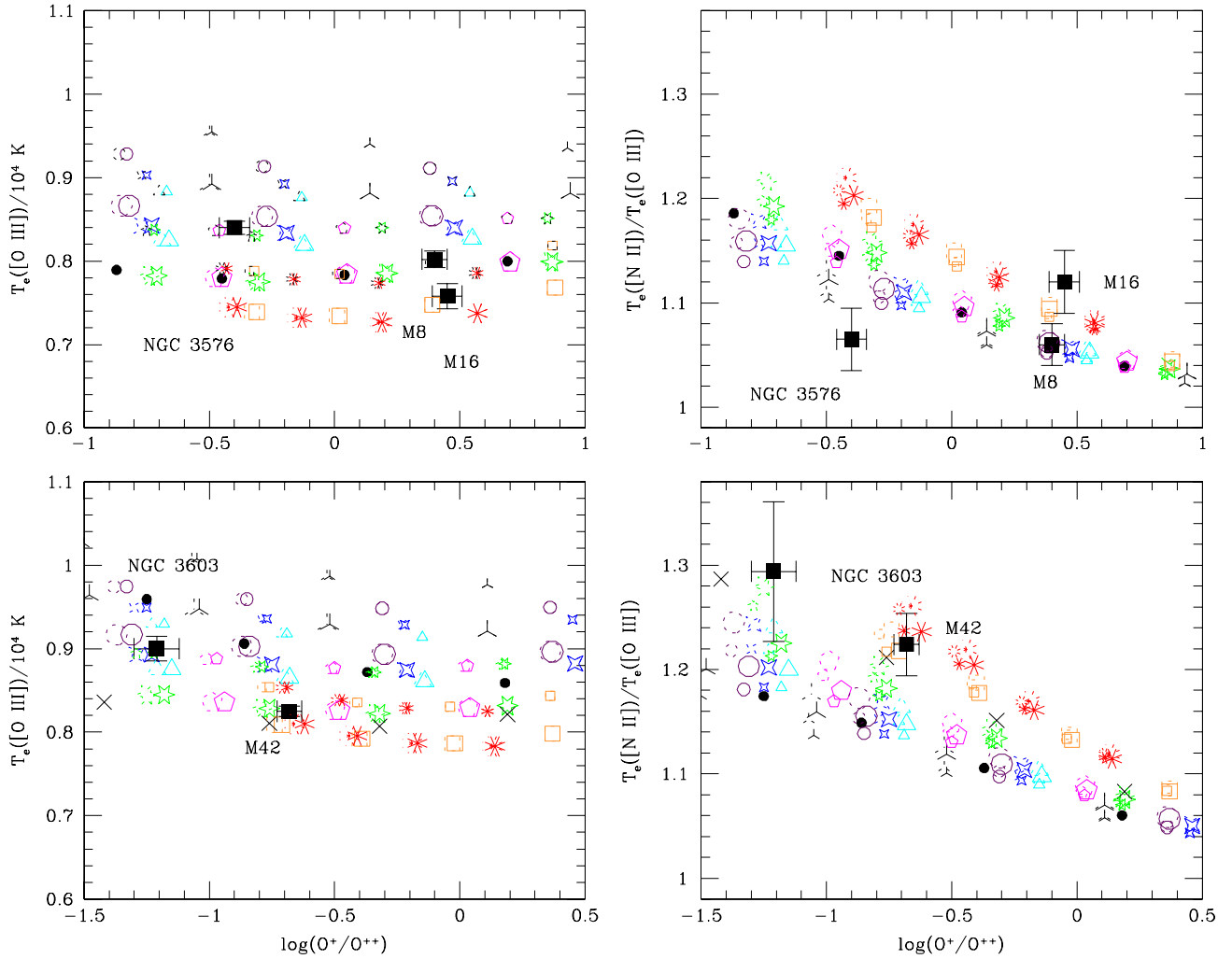
Figure 2. Values of $T_e([O\,III])$ and $T_e([N\,II])/T_e([O\,III])$ for observed objects (filled black squares) and photoionization models (other symbols). The models have $n_H = 1000\ cm^{-3}$ (top panels) or $5000\ cm^{-3}$ (bottom panels), and $T_{eff} = 35{,}000$ K (red asterisks), 37,000 K (orange open squares), 39,000 K (green six-pointed stars), 41,000 K (cyan triangles), 43,000 K (blue four-pointed stars), 45,000 K (violet circles), 50,000 K (black inverted Ys), or both $T_{eff} = 35{,}000$ K and 45,000 K (magenta pentagons). Big symbols correspond to models with $12 + \log(O/H) = 8.6$; small symbols have $12 + \log(O/H) = 8.5$. Dotted symbols show values derived considering the contribution of recombination to the intensity of [N II] $\lambda 5755$. The small filled circles show the effects of decreasing the metallicity of the ionizing stars by a factor of 2 (top panels) and of changing the dust grains from "Orion" type to "ISM" type (bottom panels) for models with $T_{eff} = 39{,}000$ K and $12 + \log(O/H) = 8.6$. Models with $T_{eff} = 39{,}000$ K and $12 + \log(O/H) = 8.6$ but with no grains included are shown as crosses in the bottom panels. See the text for more explanations.

(A color version of this figure is available in the online journal.)

4.3. Changing the Metallicity of the Ionizing Star

All the calculations were performed with stellar spectra for solar metallicity, with $12 + \log(O/H)_\odot \gtrsim 8.7$ (e.g., Scott et al. 2009 and references therein). However, the models have input metallicities in the range $12 + \log(O/H)_\odot = 8.3\text{–}8.6$. We calculated four new models with $n_H = 1000\ cm^{-3}$ and $12 + \log(O/H) = 8.6$, ionized by stars with $T_{eff} = 39{,}000$ K and half-solar metallicity, and with $\log u = -3.0\ -2.5, -2.0$, and -1.5. The results of these models are plotted as small filled circles in the top panels of Figure 2. The new models have a higher degree of ionization but show a similar behavior to the original ones.

4.4. Effect of Dust Grains

The models include dust grains, and the grains affect the temperature, mainly through heating by the photoelectric effect. The fractional contribution of grains to the heating increases with the ionization parameter and decreases with the effective temperature of the ionizing star. For the main photoionization models described so far, the contribution can be negligible or reach $\sim 30\%$ of the global heating. We are using the "H II region" (or "Orion") dust grains, a mixture of graphite and silicate grains that is deficient in small particles in order to explain the gray extinction in M42 (Baldwin et al. 1991), but there are many uncertainties related to which grains would be suitable. Changing the type of dust grains will change the temperature structure. To illustrate this effect, we calculated four new models with $n_H = 5000\ cm^{-3}$, $12 + \log(O/H) = 8.6$, $T_{eff} = 39{,}000$ K, and $\log u = -2.5, -2.0, -1.5$, and -1.0, changing the type of dust from "H II region" to "ISM". The "ISM" dust grains are also composed of graphite and silicate, but have a size distribution that includes small grains. The results of these models are plotted as small filled circles in the bottom panels of Figure 2. They have higher values of $T_e([O\,III])$ and lower values of $T_e([N\,II])/T_e([O\,III])$. Whereas the original models (with $T_{eff} = 39{,}000$ K, $12 + \log(O/H) = 8.6$, and "H II region" dust) had 8% as the maximum contribution of grains to the global heating, the new models reach 30%. Note, however, that the results are not very different from the original ones.

The same test models were computed with no grains included (but keeping the depleted abundances of refractory elements). These models show lower values for the derived electron temperatures and higher values of $T_e([N\ II])/T_e([O\ III])$ than the original ones. This is shown by the crosses in the bottom panels of Figure 2.

One of our objects, 30 Doradus, is located in the LMC, where dust grains can be very different from Galactic grains. However, the amount of dust in 30 Doradus is probably well reproduced by the comparison models of the bottom panels in Figure 1. All our models have high depletion factors of refractory elements onto dust grains, and the depletion factors are kept constant by scaling together the abundances of metals and grains. If we consider iron a good representative of refractory elements, this assumption is supported by the high iron depletion factors found in 30 Doradus and several Galactic H II regions (Rodríguez & Rubin 2005). On the other hand, the grains in 30 Doradus could have a different composition and be smaller than their Galactic counterparts (see Sloan et al. 2008 and Paradis et al. 2009 for some recent results), but the effects of the different characteristics of grains in 30 Doradus on the calculated temperatures are likely to be of the order of those discussed above. For a more thorough investigation of the effects of changes in composition and size distribution on model output, see van Hoof et al. (2004).

4.5. Advection

The models we are calculating are static. In the dynamical case, the ionization of neutral material entering the ionization front (advection), can increase the temperature of the gas in that region (e.g., Rodríguez-Gaspar & Tenorio-Tagle 1998). This will translate into higher values of $T_e([N\ II])$, but the effect is probably small, as discussed by Henney et al. (2005).

5. RESULTS FOR THE CASE WITH EXTRA HEATING

We have shown that the grids of simple photoionization models reproduce very well the temperatures and metallicities implied by the intensities of CELs relative to hydrogen RLs in the observed objects. However, these models have $ADF(O^{++}) \simeq 1.1$ and hence do not reproduce the intensities of O II RLs. In order to reproduce the intensities of both CELs and RLs, some extra ingredient must be added to the models. What characteristics should this extra ingredient have so that it does not destroy the agreement found so far between observations and models?

We start exploring the case where the extra ingredient is a heating agent that acts in some regions of the nebula producing temperature fluctuations. In this case, the emission of CELs will be strongly biased toward the hotter regions leading to overestimates of the derived temperatures and underestimates of the abundances. The abundances derived using O II RLs and the temperature fluctuations formalism first developed by Peimbert (1967; see also Peimbert et al. 2004, and references therein) will be more reliable. As an example, in M8 and M16, the oxygen abundances derived with this procedure are $12 + \log(O/H) \simeq 8.7$–8.8 (García-Rojas et al. 2006, 2007).

We modified the function that can be used to introduce a term of extra heating in Cloudy so that the term was only added at localized depths within the ionized slab. In this way, we can produce spikes in the temperature structure of the ionized region: the spikes appear in those zones where the term of extra heating is different from zero. The approach is somewhat similar to the one used by Binette et al. (2001). The temperature fluctuations
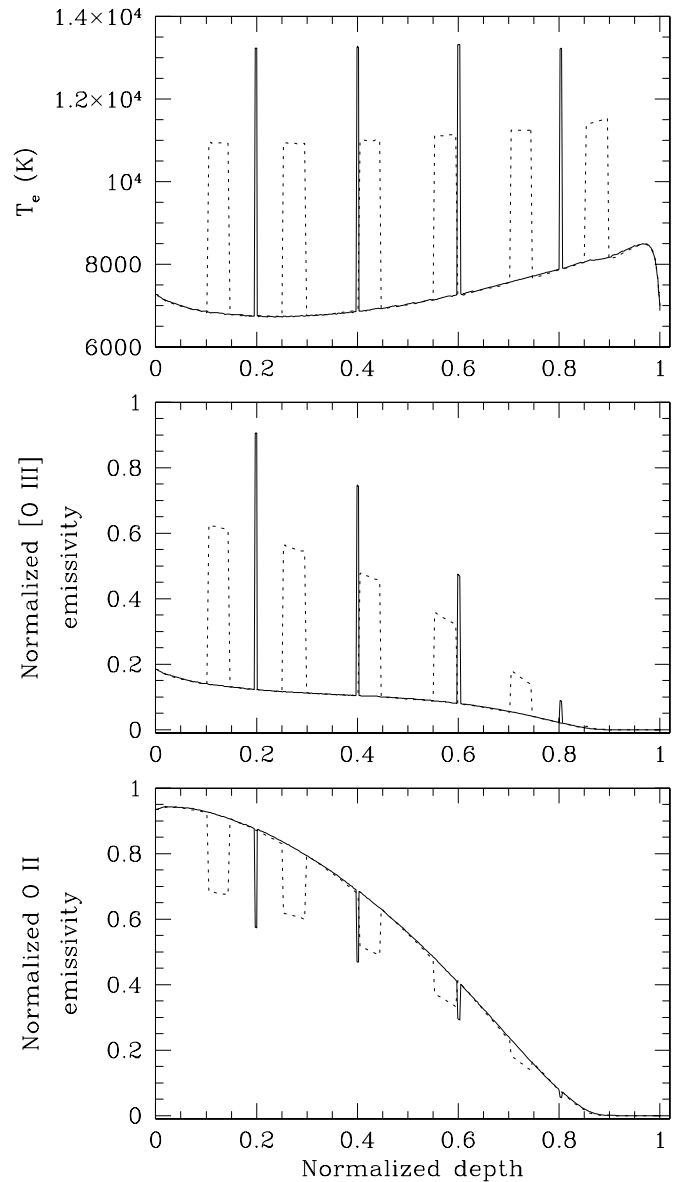

Figure 3. Upper panel: values of T_e for two models with terms of extra heating added in selected regions, as a function of normalized depth into the ionized slab (with depths of 2.49×10^{17} cm for the model plotted with a solid line and 2.66×10^{17} cm for the model plotted with a dotted line). Both models have $T_{eff} = 39,000$ K, $\log u = -2.5$, $n_H = 1000$ cm^{-3}, and input $12 + \log(O/H) = 8.75$. Both models produce $ADF(O^{++}) \sim 2$. Middle and lower panels: emissivities of [O III] $\lambda 5007$ and multiplet 1 of O II for the same models in arbitrary units.

due to these spikes introduce a bias in the temperatures and abundances derived from CELs that in turn produce values of $ADF(O^{++})$ significantly larger than 1. Note that as long as the spikes are regularly distributed across the ionized region, models with many thin spikes lead to results similar to those obtained from models where these spikes are grouped producing fewer, but broader, spikes. If one fixes the total number of spikes appearing in the ionized slab, the required values for the ADF can be obtained by varying the amount of extra heating through changes in the width or the height of the spikes.

The upper panel of Figure 3 shows the temperature structure of two models that produce $ADF(O^{++}) \simeq 2$ for some of the conditions suitable to describe M8 or M16. The middle and lower panels of Figure 3 show for these two models the emissivities of [O III] $\lambda 5007$ and multiplet 1 of O II with arbitrary
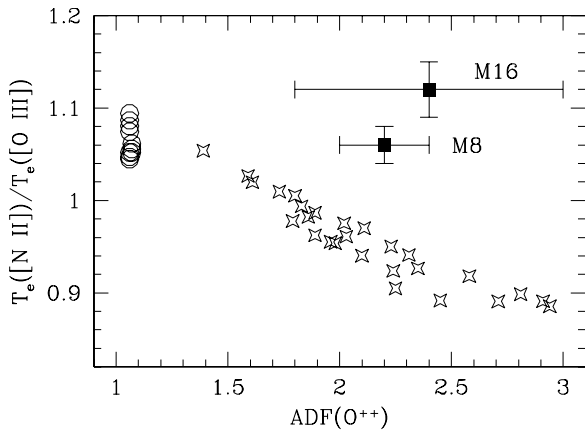
Figure 4. Values of $T_e([\text{N II}])/T_e([\text{O III}])$ as a function of ADF(O^{++}) for models with T_{eff} = 39,000 K, log u = −2.5, n_H = 1000 cm^{-3}, input 12+log (O/H) = 8.75, and temperature spikes of different thickness and widths (four-pointed stars). Also plotted are those models from the top panels in Figure 2 that have log (O$^+$/O^{++}) ∼ 0.45 (open circles), a value similar to those shown by M8 and M16 (plotted with filled squares).

normalization. Since the models have almost constant electron densities, the emissivities are modulated by the ionization fraction of O^{++} and by the electron temperature. These models illustrate how large the temperature fluctuations must be in order to produce the required ADFs. The models have T_{eff} = 39,000 K, log u = −2.5, n_H = 1000 cm^{-3}, and input 12 + log (O/H) = 8.75. Derived values are: log (O$^+$/O^{++}) ≃ 0.4, 12 + log (O/H) = 8.56 and 8.60 (for the models with the broad and thin spikes, respectively), and $T_e([\text{N II}])$ = 9300 K, $T_e([\text{O III}])$ = 9800 K (broad spikes), $T_e([\text{N II}])$ = 8000 K, $T_e([\text{O III}])$ = 8200 K (thin spikes). In the model with broad spikes, the extra heating contributes 32% of the model's total heating; in the model with thin spikes, this contribution is just 6%.

Models with a term of extra heating just 20% lower than the one used for the model with broad spikes in Figure 3 do not have enough temperature fluctuations to reach ADF(O^{++}) ∼ 2: they have ADF(O^{++}) ≲ 1.8 for spikes of any width. On the other hand, we did not explore models with terms of extra heating larger than the one used for the model with thin spikes in Figure 3. Those models would require very short integration steps in Cloudy. Besides, the thin spikes would dissipate very quickly, as discussed below.

The result found for the two models in Figure 3, $T_e([\text{N II}])$ < $T_e([\text{O III}])$, is characteristic of all the models that can be constructed in this way to produce large ADFs. This can be seen in Figure 4, where we plot the values of $T_e([\text{N II}])/T_e([\text{O III}])$ as a function of ADF(O^{++}) for several models with temperature spikes of different thicknesses and widths. Also shown are the values derived for the original models with no extra heating and plotted in the top panels of Figure 2 with log (O$^+$/O^{++}) ∼ 0.45 (a similar degree of ionization to the ones found in M8 and M16). None of the models with extra heating can reproduce the observed values of the temperature ratio, both because the extra heating tends to make similar the average temperatures of the [N II] and [O III] emitting regions, and because the [O III] diagnostic ratio is more sensitive to increments in temperature than the [N II] ratio. In order to get $T_e([\text{N II}])$ > $T_e([\text{O III}])$ as in the observed objects, the term of extra heating would have to increase with depth into the cloud. This explanation of the ADF would also work if the temperature spikes are created continuously across the full ionized region but dissipate more

easily in the regions closer to the star. Any attempt to explain the abundance discrepancy with temperature fluctuations due to extra heating would need to explain this effect in a natural way.

The results described in this section are based on illustrative but unrealistic models. The pressure differences introduced by the high-temperature regions would produce instabilities, and pressure equilibrium would be reached in times given by the ratio of the width of the spikes to the speed of sound in the gas (∼10 km s^{-1}). Hot regions with widths of 10^{15} cm, like the ones in the model with thin spikes in Figure 3, would have dynamical lifetimes of ∼30 yr. Heating and cooling processes have similar timescales in ionized gas (Osterbrock & Ferland 2006). Hence, the mechanism responsible for the hot spikes should renew them within this timescale, as previously noted by Ferland (2001).

6. COMMENTS ON MODELS THAT INCLUDE COLD GAS

Models that reproduce the intensities of O II RLs can also be built by adding a component of cold gas that contributes significantly to the emission of RLs but not to the emission of CELs. This cold gas could arise from the photoioniza-tion of metal-rich inclusions (see Tsamis & Péquignot 2005; Stasińska et al. 2007, for H II regions) or could be gas ionized by X-rays (Ercolano 2009) or cosmic rays (Giammanco & Beckman 2005). Because the cold gas is poor in hydrogen or be-cause its ionization fraction of O^{++} is larger than the one for H$^+$, CELs will give better estimates of the metallicity in the mod-els with cold gas that have considered this issue (see Stasińska et al. 2007; Ercolano 2009). To explain the ADF, the gas should have a significant fraction of O as O^{++} and a temperature low enough to suppress the emission of CELs. Some of the tem-peratures considered in the works mentioned above for the cold component have values T_e ≳ 4000 K, not low enough to prevent some emission from CELs, especially in the [N II] lines (see, for example, Figure 2 in Tsamis & Péquignot 2005). This emis-sion will lower the value of $T_e([\text{N II}])/T_e([\text{O III}])$ and hence can destroy the agreement between observations and models. There are many uncertainties related to the physical conditions of the hypothetical cold gas, and if its temperature is low enough, its emission will not contribute to CELs significantly. Hence, the observed values of $T_e([\text{N II}])/T_e([\text{O III}])$ can be used as a further constraint on this kind of explanations.

7. DISCUSSION

Typical H II regions have a zone close to the ionizing star where O^{++} is the main ionization state of oxygen and a zone where O$^+$ dominates (and where most of N$^+$ is also to be found). The stellar radiation field that determines this ionization structure heats the gas mainly through the ionization of neutral hydrogen. The excess energy carried away by the ejected electrons increases with distance from the ionizing star because the photoionization cross section of hydrogen is strongly peaked at the threshold energy of 13.6 eV, and the preferred absorption of photons with these energies hardens the ionizing radiation field. The gas cools mainly through recombination and through the collisional excitation of low-lying energy levels of abundant ions of heavy elements, responsible for the production of CELs. At each point, an equilibrium temperature is reached through the balance of all the heating and cooling processes. In this way, the temperature and the metallicity of the gas are inextricably related. The hardening of the radiation field at increasing distances from the ionizing star and the very efficient cooling provided by the [O III] lines produce a temperature gradient that

translates into the measured values of $T_e([N\,\textsc{ii}])/T_e([O\,\textsc{iii}]) > 1$ (Stasińska 1980; Osterbrock & Ferland 2006). Finally, the total emission in CELs like [O II] and [O III] lines is determined by both the ionization structure and the temperature structure of the nebula.

The ADF found between the abundances implied by [O III] CELs and O II RLs not only introduces an uncertainty in the absolute value of the gas metallicity in observed nebulae; it might also require for its explanation significant modifications of the temperature structure predicted by simple photoionization models. Therefore, a comparison between the temperature structures and metallicities measured in observed objects and predicted by simple models can give indications of how much modification the models can accommodate.

If we tried to build realistic models of the observed regions, we would need to specify several, very difficult to know, pieces of information such as the shape and luminosity of the ionizing radiation field emitted by each massive star in the region, the distance of all of these sources to the observed area, the amount and distribution of the intervening material between the ionizing sources and the observed area, and the density distribution of material in the observed area. Instead, our approach has been to construct grids of simple models and to see whether they reproduce the trends defined by complex real objects. To minimize the uncertainties related to the measurement of line intensities, we use some of the best spectra available for H II regions. We compare the temperatures, $T_e([N\,\textsc{ii}])$ and $T_e([O\,\textsc{iii}])$, and the oxygen abundances derived with the observed CELs with those derived following exactly the same procedure for grids of simple photoionization models with parameters that should encompass the ones that characterize the observed objects. The models are not tailored to reproduce any object; they just use the best guesses in Cloudy for some parameters plus state-of-the-art model atmospheres. These models reproduce easily the observed values of the temperatures and the temperature structure measured by the ratio $T_e([N\,\textsc{ii}])/T_e([O\,\textsc{iii}])$ when their input metallicities are close to those derived from CELs in the observed objects.

We also consider some modifications to the simple models so that they also reproduce the observed O II RLs. We find that temperature fluctuations introduced by some extra heating mechanism will destroy the agreement found for the simple models by decreasing $T_e([N\,\textsc{ii}])/T_e([O\,\textsc{iii}])$ to values below the observed ones. This problem might be fixed if the extra heating mechanism happens to be more efficient at larger distances from the ionizing star. On the other hand, explanations of the ADF based on the addition of cold gas in metal-rich inclusions or ionized by X-rays or cosmic rays will only work if the temperature of this gas is so low that practically no CELs arise from the inclusions. None of these types of explanations of the ADF have been shown to work at the moment, and without more details on the mechanism behind the discrepancy, we can only provide these constraints that a successful explanation should meet.

In view of the very good agreement found between the simple models and the observed objects, another explanation of the ADF in H II regions should be considered, namely, that the discrepancy is due to errors in the recombination coefficients for O II. Some authors rule out this explanation because it would lead to similar values of the ADF in all the objects, and though all H II regions and many planetary nebulae have $ADF(O^{++}) \simeq 2$, some planetary nebulae have values that go up to 70 (Liu 2006). However, note that this does not rule out

the possibility that the lower values of the ADF, found in H II regions and many planetary nebulae, can be explained in this way. Consider the Orion nebula, M42, the H II region with the best-quality spectrum and hence the one where the measured ADF is more reliable. Multiplet 1 implies $ADF(O^{++}) = 1.5$ but other multiplets that should give reliable values of the ADF imply $ADF(O^{++}) = 1.04$–1.77 (Esteban et al. 2004). The same multiplets imply $ADF(O^{++}) = 1.5$–2.3 in NGC 3576 (in the other nebulae only 1–3 reliable multiplets were measured). If the recombination coefficients are underestimated by factors around or above 1.5; and if we also consider the uncertainties related to the measurement of these very weak lines, the derived ADFs could be easily explained in H II regions and those planetary nebulae with similar ADFs. A different explanation would only be needed for the handful of planetary nebulae that show high ADFs.

On the other hand, the ADFs derived for other ions like C^{++}, although much more uncertain than those derived for O^{++}, are usually larger than 1 and correlate roughly with $ADF(O^{++})$ (see, e.g., Figure 18 in Wang & Liu 2007 for results on planetary nebulae). If the recombination coefficients for O^{++} are underestimated, the same could happen with these ions. A revision of all these recombination coefficients would be valuable.

Real nebulae are likely to have heating mechanisms besides those considered in models, and maybe some cold gas (due to shadows or ionized by alternative sources). This will introduce larger temperature fluctuations than those produced by simple models. In fact, the temperatures based on the Balmer or Paschen discontinuities of hydrogen seem to be significantly lower than those derived using CELs in some H II regions (see, e.g., García-Rojas et al. 2004, 2006). However, in other H II regions, the temperatures implied by the hydrogen discontinuities and by CELs are fully consistent (Esteban et al. 2004; García-Rojas et al. 2005). The issue is far from being settled because the hydrogen temperatures are difficult to measure and have large uncertainties. But even if real objects have more temperature fluctuations than those predicted by models, most of the ADF could still arise from errors in the recombination coefficients.

8. CONCLUSIONS

We have constructed sets of simple photoionization models with parameters that encompass those of nine H II regions, chosen because their observed spectra are of high quality. Models and observations are analyzed in the same way to derive temperatures and oxygen abundances using the relative intensities of CELs and hydrogen RLs. The good agreement found between observations and models suggests that the models capture the main characteristics of the observed objects. In particular, the agreement between the derived and predicted values of $T_e([N\,\textsc{ii}])/T_e([O\,\textsc{iii}])$ implies that the temperature structure of the observed objects is reproduced by the models. Since the [N II] and [O III] diagnostic lines used to derive T_e will react differently to changes in the temperature structure, this agreement places strong constraints on the modifications or new ingredients that can be added to the models to explain the O II RLs.

The most straightforward explanation of the ADF in H II regions (and those planetary nebulae with $ADF(O^{++}) \simeq 2$) requires errors by this amount in the recombination coefficients of O II RLs. However, we cannot rule out neither that there are relatively large temperature fluctuations due to some unknown heating mechanism whose efficiency increases with depth into

the ionized cloud nor the presence of cold ionized gas if its temperature is low enough to suppress all emission in CELs. But whatever mechanism is invoked to explain the ADF, not only should it have a plausible origin, it should also satisfy the stringent constraints imposed by the observed temperature structures.

REFERENCES

Baldwin, J. A., Ferland, G. J., Martin, P. G., Corbin, M. R., Cota, S. A., Peterson, B. M., & Slettebak, A. 1991, ApJ, 374, 580
Binette, L., Luridiana, V., & Henney, W. J. 2001, RevMexAA Conf. Ser., 10, 19
Ercolano, B. 2009, MNRAS, 397, L69
Esteban, C., Peimbert, M., García-Rojas, J., Ruiz, M.-T., Peimbert, A., & Rodríguez, M. 2004, MNRAS, 355, 229
Ferland, G. J. 2001, PASP, 113, 41
Ferland, G. J., Korista, K. T., Verner, D. A., Ferguson, J. W., Kingdon, J. B., & Verner, E. M. 1998, PASP, 110, 761
García-Rojas, J., Esteban, C., Peimbert, M., Costado, M. T., Rodríguez, M., Peimbert, A., & Ruiz, M.-T. 2006, MNRAS, 368, 253
García-Rojas, J., Esteban, C., Peimbert, A., Peimbert, M., Rodríguez, M., & Ruiz, M.-T. 2005, MNRAS, 362, 301
García-Rojas, J., Esteban, C., Peimbert, A., Rodríguez, M., Peimbert, M., & Ruiz, M.-T. 2007, RevMexAA, 43, 3
García-Rojas, J., Esteban, C., Peimbert, M., Rodríguez, M., Ruiz, M.-T., & Peimbert, A. 2004, ApJS, 153, 501
García-Rojas, J., Peña, M., & Peimbert, A. 2009, A&A, 496, 139
Giammanco, C., & Beckman, J. E. 2005, A&A, 437, L11
Henney, W. J., Arthur, S. J., Williams, R. J. R., & Ferland, G. J. 2005, ApJ, 621, 328
Lanz, T., & Hubeny, I. 2003, ApJS, 146, 417
Liu, X.-W. 2006, in IAU Symp. 234, Planetary Nebulae in our Galaxy and Beyond, ed. M. J. Barlow & R. H. Méndez (Cambridge: Cambridge Univ. Press), 219
Liu, X.-W., Storey, P. J., Barlow, M. J., Danziger, I. J., Cohen, M., & Bryce, M. 2000, MNRAS, 312, 585
Liu, Y., Liu, X.-W., Barlow, M. J., & Luo, S.-G. 2004, MNRAS, 353, 1251
Martins, F., Schaerer, D., & Hillier, D. J. 2005, A&A, 436, 1049
Osterbrock, D. E., & Ferland, G. J. 2006, Astrophysics of Gaseous Nebulae and Active Galactic Nuclei (2nd ed.; Sausalito, CA: Univ. Science Books)
Osterbrock, D. E., Tran, H. D., & Veilleux, S. 1992, ApJ, 389, 305
Paradis, D., et al. 2009, AJ, 138, 196
Pauldrach, A. W. A., Hoffmann, T. L., & Lennon, M. 2001, A&A, 375, 161
Peimbert, A. 2003, ApJ, 584, 735
Peimbert, M. 1967, ApJ, 150, 825
Peimbert, M., Peimbert, A., Ruiz, M. T., & Esteban, C. 2004, ApJS, 150, 431
Péquignot, D., Petitjean, P., & Boisson, C. 1991, A&A, 251, 680
Rodríguez, M., & Rubin, R. H. 2005, ApJ, 626, 900
Rodríguez-Gaspar, J. A., & Tenorio-Tagle, G. 1998, A&A, 331, 347
Rubin, R. H. 1986, ApJ, 309, 334
Rubin, R. H., Simpson, J. P., Haas, M. R., & Erickson, E. F. 1991, ApJ, 374, 564
Scott, P., Asplund, M., Grevesse, N., & Sauval, A. J. 2009, ApJ, 691, L119
Simón-Díaz, S., & Stasińska, G. 2008, MNRAS, 389, 1009
Sloan, G. C., Kraemer, K. E., Wood, P. R., Zijlstra, A. A., Bernard-Salas, J., Devost, D., & Houck, J. R. 2008, ApJ, 686, 1056
Stasińska, G. 1980, A&A, 85, 359
Stasińska, G. 2005, A&A, 434, 507
Stasińska, G., Tenorio-Tagle, G., Rodríguez, M., & Henney, W. J. 2007, A&A, 471, 193
Torres-Peimbert, S., & Peimbert, M. 2003, in IAU Symp. 209, Planetary Nebulae: Their Evolution and Role in the Universe, ed. S. Kwok, M. Dopita, & R. Sutherland (San Francisco, CA: ASP), 363
Tsamis, Y. G., & Péquignot, D. 2005, MNRAS, 364, 687
van Hoof, P. A. M., Weingartner, J. C., Martin, P. G., Volk, K., & Ferland, G. J. 2004, MNRAS, 350, 1330
Wang, W., & Liu, X.-W. 2007, MNRAS, 381, 669